

Characterization of Inelastic Losses
from Bose-Einstein Condensates
in the $|2, 1\rangle$ State of ^{87}Rb

Jason Merrill

April 15, 2006

Submitted to the
Department of Physics
of Amherst College
in partial fulfillment of the requirements
for the degree of
Bachelor of Arts with Distinction

Copyright © 2006 Jason Merrill

Abstract

Bose-Einstein condensates (BECs) in the $|F = 1, m_f = -1\rangle$ and $|2, 1\rangle$ states in ^{87}Rb form a unique and controllable interpenetrating superfluid system. It is important to understand and take into account the inelastic loss processes in the binary condensate in order to create an accurate numerical model of its dynamics. Loss rates due to three-body recombination have been reported previously for the $|1, -1\rangle$ state. This thesis describes a measurement of the $|2, 1\rangle$ inelastic loss rate in both condensates and thermal atoms.

Acknowledgements

First and foremost, I would like to thank my advisor, David Hall. He is a passionate experimenter whose enthusiasm is a constant inspiration. I would also like to thank our postdoc, Kevin Mertes, first for generously giving his time to help me solve countless technical problems, but more importantly for companionship in the lab.

I've had the pleasure of working with a number of other students in Professor Hall's lab over the course of two summers: Tarun Menon, Maggie McKeon, and Adam Kaplan in the summer of 2004, and Liz Petrik, Mike Goldman, and Dan Guest in the summer of 2005, and I would like to thank all of them for making those summers two of the most enjoyable I can remember. I am deeply indebted to the previous thesis students who worked to build a fantastic BEC apparatus, and on whose shoulders I am now lucky enough to stand. I would also like to thank Daniel Krause Jr., who showed me the joy of machining. Without his expertise, the apparatus could almost certainly never have been constructed. The NSF generously provided funding for this research.

Finally, I would like to thank my parents for their unconditional support.

Contents

1	Introduction	1
1.1	Bose-Einstein Condensation	1
1.2	BEC at Amherst	2
1.3	Recent Upgrades	3
1.4	Level Structure of the Rubidium Ground State	4
1.5	Previous Experiments	6
1.6	Dynamics of Overlapping Condensates	7
2	Imaging	9
2.1	Introduction	9
2.1.1	High Intensity and Off Resonance Imaging	10
2.2	Calibration	12
2.2.1	Resonant Frequency	12
2.2.2	Resonant Cross Section	12
2.2.3	Pixel Size	13
2.2.4	Saturation Intensity	16
2.2.5	Focus	17
2.3	Error Analysis	18
2.4	Additional Difficulties	20
3	Preparing A Pure $2, 1\rangle$ Sample	21

3.1	Driving A Two-Photon Transition	22
3.2	Removing Residual $ 1, -1\rangle$ Atoms	23
3.2.1	Optical Blowout Pulse	24
3.2.2	Microwave Blowout Pulse	25
3.2.3	Relative Merits	25
4	Measuring Two-Body Loss Rates in $2, 1\rangle$ atoms	28
4.1	Loss mechanisms	28
4.2	Correlations	29
4.3	Measurement	30
4.3.1	Determining Trap Lifetime	32
4.3.2	Extracting the Two-Body Loss Rate	34
4.4	Results	34
4.5	Consideration of systematic errors	38
4.5.1	Improper Saturation Correction	38
4.5.2	Improper Correction for Detuning in Condensates . . .	39
4.5.3	Overall Effect of Inaccuracies in Number	39
4.5.4	Presence of Thermal Atoms in Condensate Measurement	40
4.5.5	Thermal Clouds Not in Equilibrium	41
4.6	Conclusions	42
	Bibliography	42

List of Figures

1.1	Level structure of ^{87}Rb ground state. Magnetically trappable states are marked with a star.	5
2.1	Apparent number vs. probe aom detuning, fit to a Lorentzian. This data was taken in thermal clouds. Note that there is a difference of 2.7 MHz in resonant frequency between the $ 1, -1\rangle$ and $ 2, 2\rangle$ atoms.	13
2.2	Apparent number vs. quarter wave plate rotation. As the quarter wave plate is rotated, the atomic response goes like \cos^2 plus an offset. The minimum response is half the maximum response.	14
2.3	(a) To measure pixel size, a condensate is prepared in a weak trap, and then dropped. (b) Once the condensate has fallen below the imageable area (the dotted rectangle), the trap is briefly turned back on, tossing the condensate upward. (c) A microwave pulse is then used to transfer some of the atoms into the $ 2, 0\rangle$ state, and the trap is again briefly turned on to separate the $ 2, 0\rangle$ atoms, represented in dark grey, from the $ 1, -1\rangle$ atoms, represented in light grey with dotted borders. (d) In order to determine acceleration, the position of the $ 2, 0\rangle$ atoms is recorded at several times after the transfer.	15
2.4	Position of a tossed $ 2, 0\rangle$ condensate vs. time, fit to a parabola.	16

2.5	Plot of W vs. $N_{\text{obs.}}$. The slope of this plot is $-I_{\text{sat}}$. From this plot, $I_{\text{sat}} = 747(38)$, measured in arbitrary units of intensity (camera pixel counts).	17
2.6	Apparent peak optical depth of sub-diffraction limit condensates vs. objective position.	18
3.1	Two-photon transition. A combination of microwave and rf radiation drives the $ 1, -1\rangle \rightarrow 2, 1\rangle$ transition. The microwaves are tuned 1 MHz above the resonant frequency for the $ 1, -1\rangle \rightarrow 2, 0\rangle$ transition. The rf radiation is tuned so that the microwave and rf frequencies sum to the total frequency for the $ 1, -1\rangle \rightarrow 2, 1\rangle$ transition. In this way, the transition takes place through a virtual state (dotted), avoiding transfer of any atoms to the untrapped $ 2, 0\rangle$ state. In a 31.3 Hz radial, 87.1 Hz axial trap, the microwave and rf fields are tuned to 6.829866 GHz and 4.82335 MHz respectively.	23
3.2	Rabi oscillation between the $ 1, -1\rangle$ and $ 2, 1\rangle$ states produced by two-photon radiation.	24
4.1	Loss mechanisms. One-body losses are caused by collisions with outside atoms or photons, two-body losses primarily by spin-exchange, and three body losses primarily by molecule formation.	30
4.2	Two- and three-body loss processes cause atoms to be lost proportionally more quickly from the densest part of the cloud. As atoms rethermalize, there is a net flow of trapped atoms into the center of the cloud.	31

4.3	Measurement of the one-body loss rate k_1 , which is given by the slope of $\ln N$ vs. time. Recapture fraction is used as a proxy for number in these measurements. Fitting these plots to a line yields $k_{1 1,-1\rangle} = -6.8(7) \times 10^{-4} \text{s}^{-1}$ and $k_{1 2,2\rangle} = -7.4(4) \times 10^{-4} \text{s}^{-1}$. These loss rates translate into trap lifetimes of $\tau_{1,-1\rangle} = 25(3)$ minutes and $\tau_{2,2\rangle} = 23(1)$ minutes respectively.	33
4.4	Plots of $\ln N/N_0 - k_1 t$ vs. $k_2 \int_0^t \langle n \rangle dt$ for thermal clouds and condensates, taken in a 31.3 Hz radial, 87.1 Hz axial trap. The slopes of these plots are $k_{2\text{th}}$ and k_{2c} , the two-body loss rate for thermal clouds and condensates respectively. Condensate data was taken 10 MHz detuned, and thermal cloud data was taken on resonance. Fitting these plots to a line produces $k_{2\text{th}} = -2.34(18) \times 10^{-13} \text{cm}^3 \text{s}^{-1}$ and $k_{2c} = -1.39(5) \times 10^{-13} \text{cm}^3 \text{s}^{-1}$. Quoted errors are statistical only; systematic errors will be considered later.	35
4.5	Three-body model applied to thermal clouds in the $ 2, 1\rangle$ state. There appears to be some curvature to the residuals, but in this case it is difficult to discriminate with certainty between two- and three-body models based only on quality of fit. The three-body rate predicted by this plot is $k_{3\text{th}}$ is $-9.8(1) \times 10^{-25} \text{cm}^6 \text{s}^{-1}$, which is in poor agreement with theory.	36
4.6	Two and three-body models applied to thermal clouds in weaker trap. In this case, the two body model is clearly much better. The two-body model gives $k_{2\text{th}} = -2.60(2) \times 10^{-13} \text{cm}^3 \text{s}^{-1}$. . .	37
4.7	Plots of $\tilde{n}/\tilde{n}_{\text{calc}}$ for on resonance and off resonance imaging. In the first plot, $\Delta = 0$, and in the second, $\Delta = 3.3$	38

Chapter 1

Introduction

1.1 Bose-Einstein Condensation

Bose-Einstein Condensation (BEC) is a peculiar phase of matter which exhibits the effects of quantum mechanics on a macroscopic scale. It has been successfully created using bench-top apparatus by cooling a dilute gas of alkali atoms to ~ 100 nK. When particles with integer spin, called bosons, are cooled below a critical temperature, they begin to collect in the quantum single particle ground state of the system, which defines the onset of BEC. Because of the Pauli exclusion principle, which states that particles with half-integer spins cannot occupy the same quantum mechanical state, BEC is not possible in fermions¹.

Once cold atoms have condensed into a BEC, they display long-range coherence, meaning that the entire condensate can be viewed as a single quantum mechanical entity. Atoms in a BEC are coherent in the same way that photons in a laser are coherent. There is a definite phase relationship between atoms at one point in a condensate and atoms at any other point in the condensate.

¹At very low temperatures, fermions may pair with one another to form bosons, after which they can condense. This effect is responsible for low temperature superconductors, in which electrons form pairs called Cooper pairs, which then form a condensate.

Two effects of this coherence are that condensates can be made to exhibit interference (section 1.5), and collisions between atoms are reduced compared to a thermal sample at the same density (section 4.2).

1.2 BEC at Amherst

The construction of the Amherst BEC apparatus has been described in detail in previous theses, so I give only the briefest review here [1, 2, 3]. At Amherst, BECs are created in a dilute gas of rubidium-87 atoms. Atoms of rubidium gas are loaded into a vacuum cell by running current through a special rubidium salt, which liberates free rubidium. A magneto-optical trap (MOT) is then used to collect these atoms. The MOT uses a combination of counter-propagating lasers and magnetic field gradients to slow trapped atoms and confine them to a small space. Once they are trapped, these atoms are transferred to a second MOT which operates under ultra-high vacuum. This double MOT system has the advantage of allowing rapid collection of atoms in the first cell while dramatically reducing collisions with background gas in the second cell.

Radiation pressure due to scattered photons sets a limit on how far atoms can be cooled by a MOT. In order to achieve BEC, the atoms are loaded from the MOT into a magnetic trap. This trap takes advantage of the fact that in the presence of a magnetic field gradient, atoms with a magnetic moment anti-aligned with the field will be attracted to the minimum of the field. A field minimum is produced using coils in a quadrupole configuration.

In this configuration, the magnetic field vanishes at the center of the quadrupole coils. If atoms are allowed to reach the zero of the magnetic field, they can undergo spontaneous transitions to untrapped states, causing them to be lost. These transitions are called Majorana transitions. In order

to avoid this effect, a rapidly rotating magnetic field is added to the static quadrupole field so that the zero of the magnetic field is constantly orbiting the center of the trap. Atoms in the center of the trap will continuously feel a force toward this zero, but if it moves fast enough, they will never be able to reach it. This configuration, known as a time-averaged orbiting potential (TOP) trap, produces a 3D harmonic potential, thus trapping the atoms at the center.

Once all the atoms are loaded into the magnetic trap, the most energetic atoms are selectively evaporated using an RF field. This results in a lower average energy for the remaining cloud. As the remaining atoms undergo collisions, they rethermalize at a lower temperature. If enough atoms are initially loaded into the magnetic trap, this process eventually results in the formation of a BEC.

Once evaporation is complete, the atoms are released and allowed to undergo ballistic expansion. They are then imaged using resonant laser light (chapter 2). These images allow us to infer the momentum and density distributions of atoms while they were in the trap.

1.3 Recent Upgrades

Several important upgrades were made to the apparatus over the summer of 2006. Liz Petrick worked to refine the locking mechanism for our probe laser. In order to lock a laser beam to a spectral line, the frequency of the laser must be modulated. Previously, the frequency of the main beam was modulated. The new system works by picking off a portion of the main beam and modulating only this portion using an acousto-optic modulator (aom). Avoiding modulation of the main beam decreases the bandwidth of the probe laser, allowing better characterization of imaging. Additionally, the imaging

beam is now coupled into an angle-polished fiber which reduces shot-to-shot intensity fluctuations caused by etaloning.

Dan Guest worked to create a phase dot for use in non-destructive phase contrast imaging. This imaging technique would allow condensates to be imaged in the trap without being destroyed. It will also allow dense condensates to be imaged without the effects of lensing (see section 2.4).

Mike Goldman worked to add a new PTS 310 rapidly reprogrammable radio frequency synthesizer. This synthesizer is used to control the rf evaporation in the magnetic trap. The ability to smoothly ramp the evaporation frequency allows significantly larger condensates to be produced. Before the addition of the PTS 310, the largest condensates we commonly produced had 500,000 atoms. Now it is possible to routinely produce condensates with 800,000 or more atoms.

A new microwave frequency generator and amplifier have also been added recently. The microwave amplifier is a Microwave Power L0408-38 solid state amplifier. This amplifier replaces a Hughes Aircraft traveling wave tube amplifier. The addition of this solid state amplifier has reduced drifts in microwave power, allowing more consistent two photon transfer (section 3.1). Having a second microwave frequency generator allows us to rapidly switch between microwave frequencies, which is useful for producing a microwave blowout pulse after driving a two-photon transition (section 3.2.2).

1.4 Level Structure of the Rubidium Ground State

The ground state of ^{87}Rb is split into two hyperfine levels because of the coupling between the total angular momentum of the valence electron, J , and the total nuclear angular momentum, I . The total atomic angular momentum,

F , can take values in integer steps such that

$$|J - I| \leq F \leq |J + I|. \quad (1.1)$$

For ^{87}Rb , $I = 3/2$, and in the ground state, $J = 1/2$. This means $F = 1$ or $F = 2$. The projection of F along the quantization axis, m_f can take values in integer steps between $-F$ and F . The hyperfine state of atoms will hereafter be notated as $|F, m_f\rangle$, so an atom in the $|2, 1\rangle$ state has $F = 2$, $m_f = 1$. In the presence of a magnetic field, sub-states with different values of m_f become degenerate due to Zeeman splitting. Figure 1.1 shows the energy level structure of the ^{87}Rb ground state in the presence of a magnetic field.

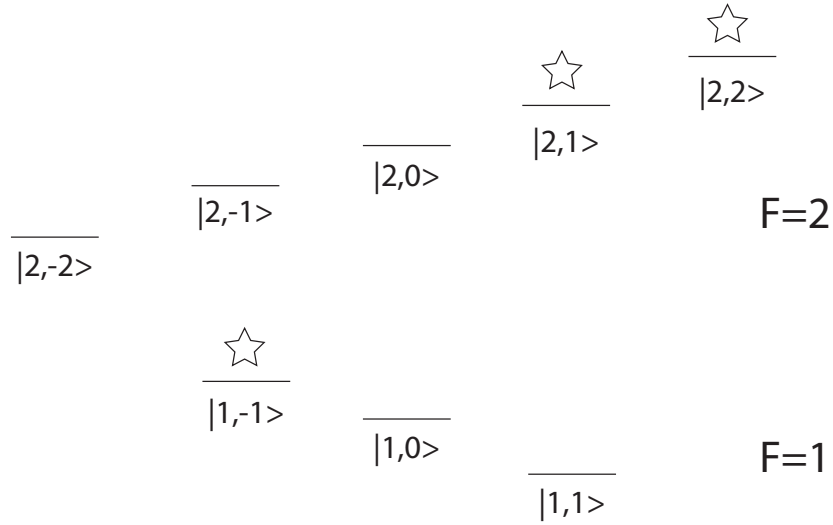


Figure 1.1: Level structure of ^{87}Rb ground state. Magnetically trappable states are marked with a star.

To first order in the magnetic field B , the energy splitting due to the Zeeman shift is $\Delta E = -g_f m_f \mu_B B$, where μ_B is the Bohr magneton and g_f is the Landé g factor, which is $1/2$ for the $F = 1$ level and $-1/2$ for the $F = 2$ level. In the presence of a magnetic field gradient, atoms with a positive ΔE feel a force in the direction of decreasing magnetic field, atoms with negative ΔE feel a force toward the magnetic field maximum, and atoms for which $\Delta E = 0$ feel no force at all. Since it is possible to create a magnetic field minimum in free space, but not a magnetic field maximum, only low-field seeking atoms are magnetically trappable. For ^{87}Rb , the $|1, -1\rangle$, $|2, 1\rangle$, and $|2, 2\rangle$ states are magnetically trappable, and the other states are not [4]. Of these three states, only the $|1, -1\rangle$ and $|2, 2\rangle$ states are suitable for evaporative cooling because of their relatively small inelastic loss rates.

1.5 Previous Experiments

Though it is difficult, or perhaps even impossible, to reach BEC through evaporative cooling of $|2, 1\rangle$ atoms, it is possible to create a condensate of atoms in the $|2, 1\rangle$ state by transferring atoms from a $|1, -1\rangle$ condensate using a two-photon transition. This process is described in further detail in section 3.1. Since $|1, -1\rangle$ atoms and $|2, 1\rangle$ atoms have the same magnetic moment, both states can simultaneously be trapped at the same position in a magnetic trap. Because of this, driving a two-photon transition in $|1, -1\rangle$ atoms allows observation of a system of interpenetrating superfluids in which the relative population of the two states can be easily controlled.

This system was first created by groups at JILA, where it was used to study the response of a condensate to a sudden change in internal state [5], the evolution of relative phase between the two states [6], and the dynamics of distinguishable interpenetrating superfluids [7].

Two-photon transfer was first used at Amherst to study interference between independently prepared condensates. In this experiment, independent condensates were simultaneously prepared in the $|1, -1\rangle$ and $|2, 2\rangle$ states. The $|1, -1\rangle$ atoms were then transferred into the $|2, 1\rangle$ state where they could be coupled to the atoms in the $|2, 2\rangle$ state using radio frequency radiation. When the atoms were allowed to interact through this coupling, interference fringes appeared on the density distributions of the condensates [8]. A similar interference experiment had previously been conducted at MIT using two separately prepared condensates in the $|1, -1\rangle$ state of sodium [9]. Interference experiments such as these dramatically demonstrate the coherence of the condensed state, and the wave-like nature of matter.

1.6 Dynamics of Overlapping Condensates

The dynamics of a system of overlapping $|1, -1\rangle$ and $|2, 1\rangle$ condensates are currently being further investigated at Amherst. When imaged along the magnetic field axis (from the top), a changing pattern of rings is observed in the density distributions of the individual states. The total density of the combined states, however, appears to remain nearly constant. By comparing the observed dynamics with numerical models, this system provides a detailed test of theory. It may be possible to extract accurate values of the three relevant atomic scattering lengths, the parameters that characterize low temperature collisions, from these comparisons.

In models of these dynamics, inelastic losses due to inter- and intra-species collisions must be taken into account. Inelastic losses in the $|1, -1\rangle$ state have been previously experimentally characterized [10]. Inelastic losses in the $|2, 1\rangle$ state, however, have not previously been characterized. This thesis attempts to experimentally determine the inelastic loss rate due to interspecies collisions in

the $|2, 1\rangle$ state. Understanding these loss processes will allow us to place tighter constraints on the numerical models of overlapping condensate dynamics.

Chapter 2

Imaging

2.1 Introduction

The most common tool used to probe condensates in this thesis is absorption imaging. In absorption imaging, we shine resonant or near resonant laser light on the cloud, which impresses a shadow on the beam. The density distribution of the cloud is inferred by imaging this shadow with a Charge-Coupled Device (CCD) camera.

For low intensity, on resonance light, the differential change in intensity as light passes through an atomic medium is given by Beer's Law:

$$\frac{dI}{dz} = -In\sigma_0, \quad (2.1)$$

where σ_0 is the resonant cross section of the atomic transition, and n is the density of atoms. Integrating this equation gives

$$\ln \frac{I_{\text{out}}}{I_{\text{in}}} = -\tilde{n}\sigma_0, \quad (2.2)$$

where \tilde{n} is the density integrated along the path of the light. The optical depth, OD , is defined as

$$OD = -\ln \frac{I_{\text{out}}}{I_{\text{in}}}. \quad (2.3)$$

In order to do quantitative imaging, three pictures are used: a dark picture D taken with the probe laser off, a shadow picture S taken while shining the laser on the cloud, and a light picture L taken with the laser on, but no cloud present. This gives

$$I_{\text{in}} = L - D \quad (2.4)$$

$$I_{\text{out}} = S - D \quad (2.5)$$

$$OD = -\ln \left(\frac{S - D}{L - D} \right). \quad (2.6)$$

The total number of atoms in a cloud can be found by solving for the column density and integrating, or in this case, summing over pixels in the camera:

$$N = \frac{A}{\sigma_0} \sum_{\text{pixels}} OD. \quad (2.7)$$

Here, A is the area of each pixel in object space—that is, the area of the cloud imaged by each pixel.

2.1.1 High Intensity and Off Resonance Imaging

Two important effects can modify the relationship between optical depth and column density: saturation, and detuning from resonance.

Saturation occurs because there is a maximum rate at which atoms can scatter photons. Once an atom absorbs a photon, it is in an excited state and cannot absorb another photon until it has had time to decay to its initial state. Imaging with high intensity light increases signal-to-noise at the camera;

however, it becomes necessary to correct for the effects of saturation. [11, 12, 13]

Detuning the probe frequency from resonance lowers the probability that an atom will scatter a photon, thereby reducing apparent optical depth. Detuning is useful for imaging dense clouds. There is a maximum optical depth that our camera can measure. All but the smallest condensates exceed this maximum optical depth when imaged on resonance, so they are imaged off resonance in order to bring their apparent optical depth back into the range that can be imaged by the camera.

Both saturation and detuning decrease the apparent optical depth of a cloud. Taking these effects into account, eq. 2.1 becomes

$$\frac{dI}{dz} = \frac{\tilde{n}\sigma_0}{1 + \Delta^2 + I/I_{\text{sat}}}, \quad (2.8)$$

where σ_0 is the on resonance, low intensity absorption cross section, I_{sat} is the saturation intensity, and Δ is the detuning in half-line widths:

$$\Delta = \frac{\nu - \nu_0}{(\Gamma/2)}, \quad (2.9)$$

where ν_0 is the resonant frequency, and Γ is the natural line width of the transition. In the case of ^{87}Rb , $\Gamma = 6.065(9)$ MHz [14].

Integrating this new form gives

$$-\tilde{n}\sigma_0 = (1 + \Delta^2) \ln \frac{I_{\text{out}}}{I_{\text{in}}} + \frac{1}{I_{\text{sat}}} (I_{\text{out}} - I_{\text{in}}) = (1 + \Delta^2) OD + \frac{I_{\text{in}}}{I_{\text{sat}}} (1 - e^{-OD}). \quad (2.10)$$

As before, dividing by σ_0 and summing over pixels, the equation for number is

$$N = \frac{A}{\sigma_0} \sum_{\text{pixels}} \left((1 + \Delta^2) OD + \frac{I_{\text{in}}}{I_{\text{sat}}} (1 - e^{-OD}) \right). \quad (2.11)$$

2.2 Calibration

In order to make accurate measurements of number, it is first necessary to calibrate the apparatus by measuring all of the parameters in eq. 2.11: A , σ_0 , I_{sat} , and Δ (actually ν_0). A description of the methods used to measure each of these quantities follows.

2.2.1 Resonant Frequency

The resonant frequency of the probe transition is measured by observing apparent optical depth of identically prepared clouds at a series of different probe frequencies. Optical depth has a Lorentzian dependence on frequency, being largest at the resonant frequency. For the purposes of this and other calibration measurements, apparent number is used as a proxy for apparent optical depth. Recall from equation 2.7 that number is proportional to the spatial integral of optical depth, so any process that scales optical depth by the same factor over the whole image will scale number by the same factor.

The probe frequency is controlled using an aom. First, the probe frequency is locked to a nearby transition. The aom is then used to shift the probe frequency by 110–150 MHz into the range of the probe transition.

2.2.2 Resonant Cross Section

The resonant cross section of an atomic transition is the effective area over which a single atom absorbs resonant light. It is dependent on the polarization of the incoming beam. If the atoms all have their quantization axes aligned and the probe beam is optimally polarized for the transition, then the resonant cross section is

$$\sigma_0 = \frac{3\lambda^2}{2\pi}, \quad (2.12)$$

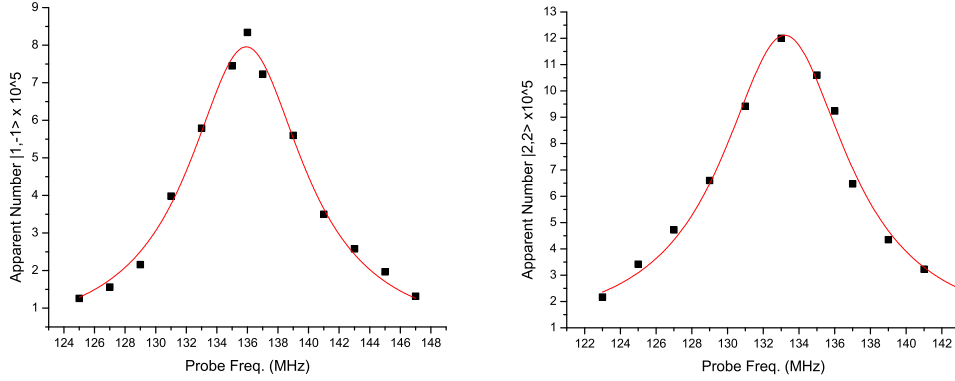


Figure 2.1: Apparent number vs. probe aom detuning, fit to a Lorentzian. This data was taken in thermal clouds. Note that there is a difference of 2.7 MHz in resonant frequency between the $|1, -1\rangle$ and $|2, 2\rangle$ atoms.

where λ is the wavelength of the transition. In order to ensure that all the atoms have their quantization axes aligned, a small rotating field of 1 gauss is used during imaging. A quarter wave plate is used to convert the linearly polarized probe beam into circularly polarized light. In order for the light to be circularly polarized in the reference frame of the atoms, the probe pulse must occur when the rotating field is aligned along the imaging axis, and the angle of the rotation of the quarter wave plate must be correct. Figure 2.2 shows a plot of apparent number vs. rotation of the quarter wave plate. [11]

2.2.3 Pixel Size

Pixel size is measured by observing the acceleration of a condensate during free fall. By comparing the acceleration measured in px/s^2 to the known acceleration due to gravity in m/s^2 , the size of a pixel in object space can be inferred. The parameter A from equation 2.11 is simply the square of this pixel size.

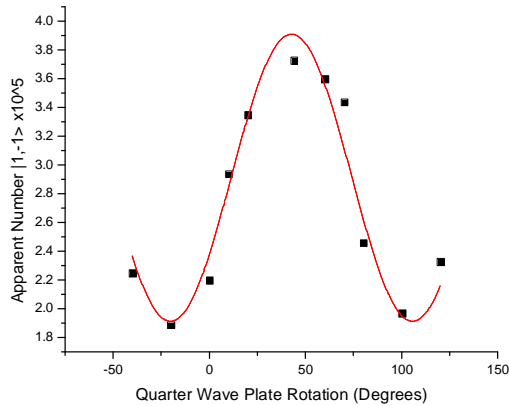


Figure 2.2: Apparent number vs. quarter wave plate rotation. As the quarter wave plate is rotated, the atomic response goes like \cos^2 plus an offset. The minimum response is half the maximum response.

A precise measurement of acceleration requires the velocity of the condensate to change significantly during the time that it can be imaged. If a condensate is simply dropped from the trap, this requirement is not met; its velocity when it reaches the top of the imageable area is large enough that it spends relatively little time in the imageable area, meaning its velocity does not change significantly. In order to solve this problem, the condensate is “tossed.” First, it is released from the trap and allowed to drop until it has gone below the bottom of the imageable area. Then, the quadrupole field is turned back on, causing the condensate to accelerate upward toward its equilibrium trap position. Once the condensate has acquired sufficient upward velocity, the trap is again turned off. In this way, the condensate can be imaged as it travels upward from the bottom of the imageable area, turns around under the influence of gravity, and then falls back down through the imageable area. Figure 2.3 shows a diagram of this measurement.

A complication arises from the possible presence of a stray magnetic field gradient, which would cause an additional acceleration in atoms in the trap-

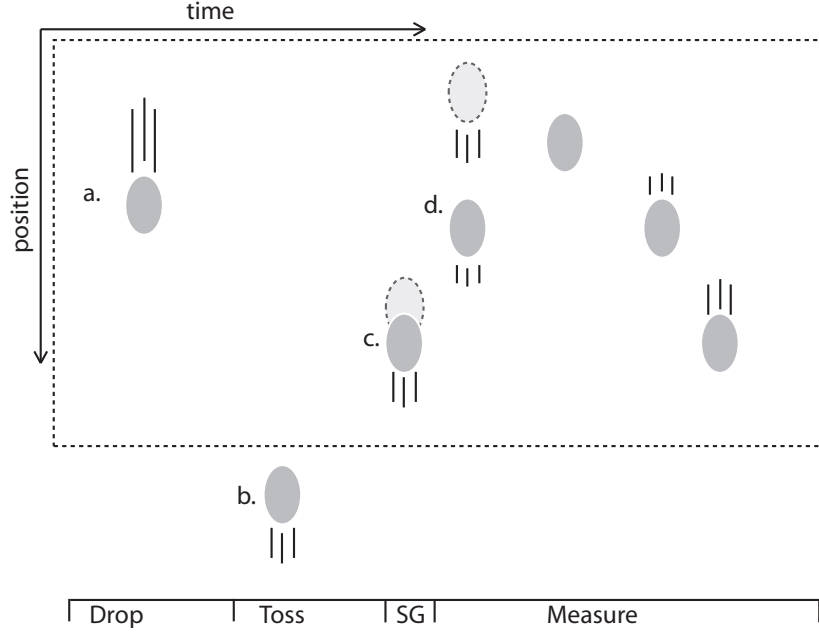


Figure 2.3: (a) To measure pixel size, a condensate is prepared in a weak trap, and then dropped. (b) Once the condensate has fallen below the imageable area (the dotted rectangle), the trap is briefly turned back on, tossing the condensate upward. (c) A microwave pulse is then used to transfer some of the atoms into the $|2,0\rangle$ state, and the trap is again briefly turned on to separate the $|2,0\rangle$ atoms, represented in dark grey, from the $|1,-1\rangle$ atoms, represented in light grey with dotted borders. (d) In order to determine acceleration, the position of the $|2,0\rangle$ atoms is recorded at several times after the transfer.

pable states. Atoms in the $|2,0\rangle$ state, however, have essentially no magnetic moment and are thus unaffected by weak field gradients.

In order to measure pixel size using $|2,0\rangle$ atoms, a condensate is first prepared in the $|1,-1\rangle$ state and tossed. After the toss, microwave radiation is used to transfer the atoms into the $|2,0\rangle$ state. The quadrupole field is then briefly turned back on, acting as a stern-gerlach gradient in order to separate the two states. The acceleration of the $|2,0\rangle$ atoms is then observed as described above. Figure 2.4 shows a plot of position vs. time for a tossed

condensate in the $|2, 0\rangle$ state.

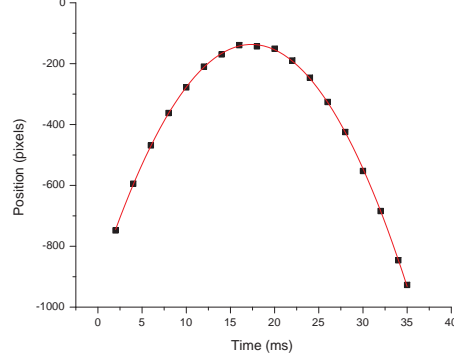


Figure 2.4: Position of a tossed $|2, 0\rangle$ condensate vs. time, fit to a parabola.

2.2.4 Saturation Intensity

In order to measure I_{sat} , a thermal cloud is imaged on resonance at varying probe intensities, and the corresponding changes in apparent number are observed. By fitting to equation 2.11, we extract I_{sat} . We rewrite equation 2.11 by renaming N as N_{true} , and defining

$$N_{\text{obs.}} = \frac{A}{\sigma_0} \sum_{\text{pixels}} OD \quad (2.13)$$

$$W = \frac{A}{\sigma_0} \sum_{\text{pixels}} I_{\text{in}}(1 - e^{-OD}). \quad (2.14)$$

$$\begin{aligned} N_{\text{true}} &= (1 + \Delta^2)N_{\text{obs.}} + W/I_{\text{sat}} \\ W &= -I_{\text{sat}}(1 + \Delta^2)N_{\text{obs.}} + I_{\text{sat}}N_{\text{true}}. \end{aligned} \quad (2.15)$$

On resonance, where $\Delta = 0$, the slope of a plot of W vs. $N_{\text{obs.}}$ is $-I_{\text{sat}}$. Figure 2.5 shows a plot of this calibration.

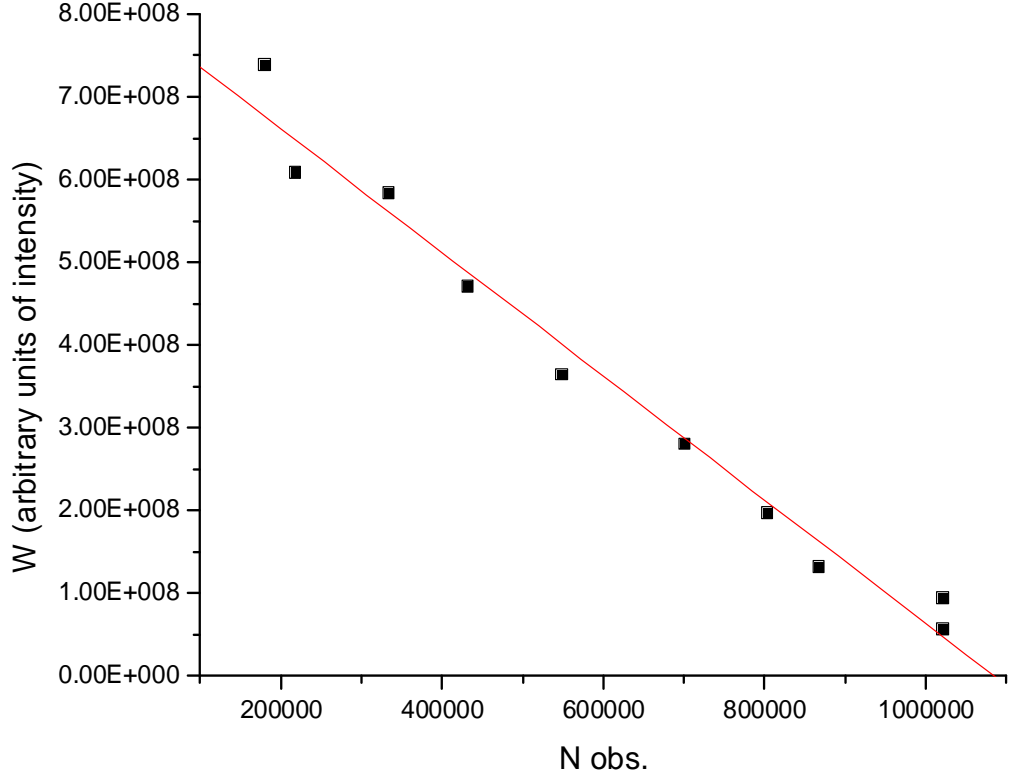


Figure 2.5: Plot of W vs. $N_{\text{obs.}}$. The slope of this plot is $-I_{\text{sat}}$. From this plot, $I_{\text{sat}} = 747(38)$, measured in arbitrary units of intensity (camera pixel counts).

2.2.5 Focus

In addition to the parameters listed above, clear images require that the shadow produced by the condensate be in focus on the camera. In order to focus the camera, condensates smaller than the diffraction limit of the optical system were produced and imaged. The further the system is from focus, the more widely dispersed these condensates will appear. In other words, as the system is focused, the apparent width of the condensate will decrease and the apparent peak optical depth will increase. Figure 2.6 shows a plot of apparent peak optical depth vs. position of the objective lens.

One difficulty associated with focusing the optical system is that clouds

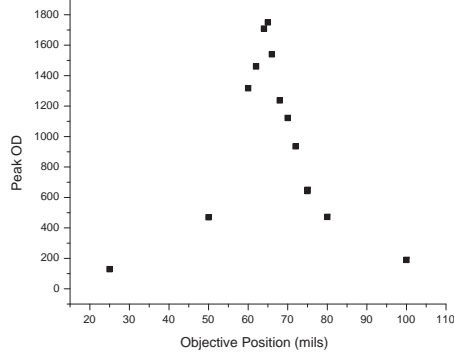


Figure 2.6: Apparent peak optical depth of sub-diffraction limit condensates vs. objective position.

may pick up some horizontal velocity when they are released from the trap. As they fall, they will pass into and then out of the plane of focus. This means that if the camera is focused using condensates prepared in a certain trap and dropped for a certain length of time, images of condensates prepared in different traps or imaged at different drop times may not be in good focus.

2.3 Error Analysis

With calibrations of all of the necessary parameters in hand, it is now possible to calculate the total systematic uncertainty in a measurement of the number. In general, for a function F of independent variables $a_0...a_n$, the standard error in F is

$$S_F = \sqrt{\sum_{i=1}^n \left(\frac{\partial F}{\partial a_i}\right)^2 S_{a_i}^2}, \quad (2.16)$$

where S_{a_i} is the standard error of a_i . Applying this formula to equation 2.11 gives the total standard error in N :

$$\frac{S_N}{N} = \sqrt{c_{I_{\text{sat}}}^2 \left(\frac{S_{I_{\text{sat}}}}{I_{\text{sat}}} \right)^2 + c_{\nu_0}^2 S_{\nu_0}^2 + c_{ps}^2 \left(\frac{S_{ps}}{ps} \right)^2 + c_{\sigma_0}^2 \left(\frac{S_{\sigma_0}}{\sigma_0} \right)^2} \quad (2.17)$$

$$c_{I_{\text{sat}}} = \frac{W/I_{\text{sat}}}{N} \quad (2.18)$$

$$c_{\nu_0} = \frac{2(\nu - \nu_0)}{(\Gamma/2)^2(1 + I/I_{\text{sat}} + \Delta^2)} \quad (2.19)$$

$$c_{ps} = 2 \quad (2.20)$$

$$c_{\sigma_0} = 1 \quad (2.21)$$

Table 2.3 lists the measured values of the imaging parameters and their standard errors.

<i>Parameter</i>	<i>Value</i>	<i>Standard Error</i>
$\nu_{0 1,-1\rangle}$	135.9 MHz	.1 MHz
$\nu_{0 2,2\rangle}$	133.2 MHz	.1 MHz
ps	1.911 $\mu\text{m}/\text{px}$.006 $\mu\text{m}/\text{px}$
σ_0	0.2907 μm^2	—
I_{sat}	747	38

Here, I_{sat} is measured in arbitrary units of intensity. Since the polarization of the probe beam is set at the top of a peak (where the derivative is zero), and since the wavelength of the probe transition is known very precisely, the standard error of σ_0 is small enough to ignore.

In order to maximize signal to noise, atoms are generally imaged using light of intensity such that $I/I_{\text{sat}} \approx 1$. Thermal clouds are commonly measured on resonance so that $\Delta = 0$. Condensates must be imaged off resonance because of their large optical depth; commonly, $\Delta = 3.4$.

For a thermal cloud with $N = 1 \times 10^6$, a typical value of W is about 3.7×10^8 . Using these values in equation 2.17, the total systematic error in measuring number in a thermal cloud of this size on resonance due to calibration uncertainty is about 2.5%. Until very recently, the saturation correction was

not implemented correctly, so typical values of W are unavailable for condensates at the time of writing. This makes a similar calculation for condensates measured off resonance impossible.

2.4 Additional Difficulties

When imaging off resonance, clouds have a density-dependent index of refraction n_{ref} ,

$$n_{\text{ref}} = 1 + \frac{\sigma_0 n \lambda}{4\pi} \left(\frac{\Delta}{1 + \Delta^2} \right), \quad (2.22)$$

causing them to behave as lenses. If clouds are perfectly in focus, in the low density limit, this lensing should not have any effect. However, there is no guarantee that clouds prepared in different ways will drop to the same position when they are imaged, so it is difficult to know whether a given cloud is perfectly in focus. If clouds are not perfectly in focus, lensing will result in distortion of the observed density distributions. The total amount of light scattered by the cloud, and thus the total measured number should not be affected by lensing unless the effect is so strong that light is bent out of the collection range of the optics. For high density clouds (i.e. condensates), it is also possible that lensing will cause bent light to be absorbed by atoms that would not otherwise have been in the path of the light. The number of atoms measured in condensates seems to depend strongly on the sign of the detuning in our system. This effect is likely somehow related to lensing, since the index of refraction is the only place that the sign of the detuning is important. This important discrepancy was only discovered recently and at the time of writing is not yet well understood.

Chapter 3

Preparing A Pure $|2, 1\rangle$ Sample

In order to measure the two-body loss rate in magnetically trapped $|2, 1\rangle$ atoms, a sample of atoms purely in this state must be prepared. The apparatus is only designed, however, to load either $|2, 2\rangle$ or $|1, -1\rangle$ atoms into the magnetic trap. This is because optical pumping tends to push atoms toward the stretched states, that is, states with the maximum allowed projection of angular momentum m_f [2]. There is no simple way to optically pump atoms into the $|2, 1\rangle$ state without also leaving atoms in the other trapped states. This means atoms must be transferred into the $|2, 1\rangle$ state after they are loaded into the magnetic trap.

One could imagine using rf radiation to drive the $|2, 2\rangle \rightarrow |2, 1\rangle$ transition. Since these states have different magnetic moments and thus different trap positions, however, driving this transition causes transferred atoms to accelerate toward their new trap position, thus gaining unwanted energy. As the atoms rethermalize in the new trap, this energy will translate into higher temperature. Instead, a two-photon transition is used to transfer atoms from the $|1, -1\rangle$ state into the $|2, 1\rangle$ state. [1, 5]

3.1 Driving A Two-Photon Transition

Since each photon carries only a single unit of angular momentum, two photons are required to transfer an atom from a state with $m_f = -1$ to a state with $m_f = 1$. To drive the $|1, -1\rangle \rightarrow |2, 1\rangle$ transition, the atoms are exposed to a combination of microwave and radio frequency radiation. The frequencies are chosen so that the energy of a microwave photon plus the energy of an rf photon is equal to the difference in energy between the $|1, -1\rangle$ and $|2, 1\rangle$ states (figure 3.1). By detuning the microwave frequency approximately 1 MHz from the $|1, -1\rangle \rightarrow |2, 0\rangle$ transition, we access a virtual state that allows passage between the $|1, -1\rangle$ and $|2, 1\rangle$ states without going directly through the $|2, 0\rangle$ state. Because the $|2, 0\rangle$ state is an untrapped state, if atoms were transferred to this state they would immediately leave the trap, which would make it impossible to further transfer them to the $|2, 1\rangle$ state.

Once the two states are radiatively coupled, the system behaves like any other two level system. The population of atoms oscillates as sine squared in time between the two states (figure 3.2). This phenomenon is known as Rabi oscillation. For typical microwave and rf powers, we observe a Rabi frequency of approximately 250 Hz.

By driving a π -pulse, it should be possible to make a complete transfer between the $|1, -1\rangle$ and $|2, 1\rangle$ states. In practice, we are only able to achieve between 90–95% percent transfer in condensates, and somewhat less in thermal clouds. Because of gravity, the exact frequency needed to drive the two-photon transition through the $|2, 0\rangle$ state varies spatially across the cloud; hence it is impossible to produce perfect transfer with only a single frequency. This effect is more pronounced in thermal clouds than in condensates because thermal clouds are physically larger. Additionally, the magnetic field variation across the cloud is greater.

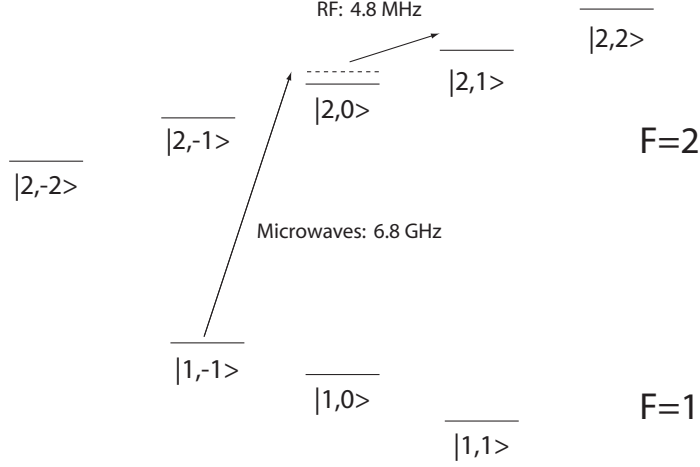


Figure 3.1: Two-photon transition. A combination of microwave and rf radiation drives the $|1, -1\rangle \rightarrow |2, 1\rangle$ transition. The microwaves are tuned 1 MHz above the resonant frequency for the $|1, -1\rangle \rightarrow |2, 0\rangle$ transition. The rf radiation is tuned so that the microwave and rf frequencies sum to the total frequency for the $|1, -1\rangle \rightarrow |2, 1\rangle$ transition. In this way, the transition takes place through a virtual state (dotted), avoiding transfer of any atoms to the untrapped $|2, 0\rangle$ state. In a 31.3 Hz radial, 87.1 Hz axial trap, the microwave and rf fields are tuned to 6.829866 GHz and 4.82335 MHz respectively.

3.2 Removing Residual $|1, -1\rangle$ Atoms

If atoms are left in the $|1, -1\rangle$ state after the transfer, interspecies collisions likely produce additional losses from the $|2, 1\rangle$ state, confusing measurements of the $|2, 1\rangle$ loss rate. At typical densities, intraspecies losses from the $|2, 1\rangle$ state are much faster than corresponding intraspecies losses from the $|1, -1\rangle$ state, so as the system evolves, the density of the $|1, -1\rangle$ atoms grows relative to the density of $|2, 1\rangle$ atoms, making the effect worse. For this reason, any atoms left in the $|1, -1\rangle$ must be removed from the trap.

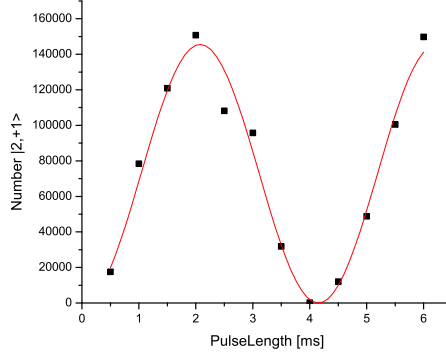


Figure 3.2: Rabi oscillation between the $|1, -1\rangle$ and $|2, 1\rangle$ states produced by two-photon radiation.

As always, there are three options for manipulating these atoms: radio frequency magnetic fields, microwave radiation, or laser light. An rf pulse could be used to transfer the remaining $|1, -1\rangle$ atoms to the untrapped $|1, 0\rangle$ state. This is what occurs during evaporation. Unfortunately, owing to the degeneracy of atomic transitions, this radiation would also transfer the $|2, 1\rangle$ atoms to the untrapped $|2, 0\rangle$ state, so this strategy is ultimately unacceptable. On the other hand, both optical and microwave transfer are useful strategies. Their implementation and relative merits are discussed below.

3.2.1 Optical Blowout Pulse

Conveniently, $F = 1 \rightarrow F' = 2$ light used for repump during the MOT phase is already available. A very short repump pulse ($500 \mu\text{s}$) is sufficient to remove any residual $|1, -1\rangle$ atoms. Unfortunately, as these energetic atoms leave they trap, they can collide with trapped atoms causing significant heating and collateral loss of $|2, 1\rangle$ atoms. The disturbance caused by this process means that clouds must be given sufficient time to return to equilibrium after the blowout pulse.

3.2.2 Microwave Blowout Pulse

It is also possible to use microwaves to drive either $|1, -1\rangle \rightarrow |2, -2\rangle$ or $|1, -1\rangle \rightarrow |2, 0\rangle$ transitions. In practice, we choose the latter transition because we find it causes less disturbance to the remaining cloud. This is unsurprising: since the $|2, -2\rangle$ state is antitrapped, transferred atoms pick up momentum from the magnetic field gradient as they leave the trap, whereas the $|2, 0\rangle$ state is simply untrapped, so atoms leave due to the relatively more gentle force of gravity. Microwave photons are much less energetic than optical photons, so atoms leaving the trap through this process cause significantly less disturbance than atoms forced out with repump light.

The disadvantage of using a microwave blowout pulse is that it is significantly slower than using an optical pulse. Because of the magnetic field gradient, the microwave transition frequency varies across the cloud. This means that only a portion of the atoms are eliminated at once. Again, this effect is worse in thermal clouds than in condensates because thermal clouds occupy a larger volume. We find that a 22 ms microwave pulse is sufficient to completely transfer thermal clouds or condensates of $|1, -1\rangle$ atoms out of the trap. As an aside, it is amusing to note that using this technique to transfer atoms out of a condensate produces a so-called atom laser. [1, 15]

3.2.3 Relative Merits

In general, the optical blowout pulse is not suitable for condensates. Due to the relatively high atomic density in a condensate, transferred atoms are more likely to collide with trapped atoms as they leave the trap. Heating produced by these collisions causes significant melting of the condensate—that is, the fraction of atoms occupying the single particle ground state is reduced. In addition, this disturbance can set up oscillations in the condensate, which

may have long relaxation times. Even when no $|1, -1\rangle$ atoms are present, repump light appears to affect the shape of a $|2, 1\rangle$ condensate, presumably due to an induced electric dipole interaction with the electric field of the laser.

Optical blowout pulses work much better in thermal clouds. Because of their relatively lower density, collisions as atoms leave the trap are less likely. In addition, heating and disturbance from equilibrium are of little concern since after the disturbance a thermal cloud will eventually re-thermalize and simply be a warmer thermal cloud.

Microwave blowout pulses are most effective in condensates because of the relatively homogeneous transition frequency, but a long pulse also appears to be effective for thermal clouds. In practice, we use a 22 ms microwave blowout pulse in both condensates and thermal clouds. Since it has no negative consequences, an optical blowout pulse is added for thermal clouds after the microwave blowout pulse to further ensure that no $|1, -1\rangle$ atoms remain.

It is difficult to gauge the effectiveness of these blowout pulses with certainty. An effective blowout pulse would be one in which, after the transfer and blowout pulse, most of the atoms are left in the $|2, 1\rangle$ state and no atoms are left in the $|1, -1\rangle$ state. In order to image $|1, -1\rangle$ atoms, an optical pumping pulse is first used to clear out any $|2, 1\rangle$ atoms. This optical pumping pulse is not perfect, however, meaning that if many $|2, 1\rangle$ atoms were present before the optical pumping pulse, some of them may be unintentionally imaged. It is thus difficult to confirm that no $|1, -1\rangle$ atoms are left behind. Instead, we use the blowout pulse procedure on thermal clouds and condensates of $|1, -1\rangle$ atoms without first transferring any of them to the $|2, 1\rangle$ state. In this case, since no $|2, 1\rangle$ atoms are present, by imaging on resonance we can confirm that no atoms are left after the blowout pulses. We then assume that if the blowout pulse is capable of removing an entire $|1, -1\rangle$ thermal cloud or con-

densate from the trap, it will also be effective at removing the small number of $|1, -1\rangle$ atoms that remain after a two-photon π -pulse to the $|2, 1\rangle$ state.

Chapter 4

Measuring Two-Body Loss Rates in $|2, 1\rangle$ atoms

Density-dependent losses are modeled very generally by the rate equation

$$\dot{n} = k_1 n + k_2 n^2 + k_3 n^3 + \dots \quad (4.1)$$

where n is the density. Terms of order m are associated with m -body processes, so the first term is associated with one-body processes, the second with two-body processes and so on. In dilute gases, densities are low enough that terms of order higher than 3 in the density typically need not be considered. The important mechanisms for one-, two-, and three-body losses are considered in the following section.

4.1 Loss mechanisms

One-body losses are caused by collisions with untrapped atoms or absorption of stray photons. Such collisions are minimized by working at ultra-high vacuum and shielding the science cell from outside light.

Two-body losses are caused by collisions between two trapped atoms that change the internal state of the atoms. At very low temperatures, where most

atoms are in the electronic ground state, there are two mechanisms that can cause changes in internal state: spin-exchange, and dipolar relaxation. Dipolar relaxation is caused by an interaction between the nuclear and electronic dipole moments of the two atoms. It is typically orders of magnitude slower than other loss mechanisms. Spin-exchange occurs when two atoms collide and exchange a unit of nuclear or electronic spin. For example, two atoms in the $|2, 1\rangle$ state could exchange a unit of spin leaving one atom in the $|2, 0\rangle$ state and the other in the $|2, 2\rangle$ state. This process conserves total F and m_f . For this reason, spin exchange is forbidden for intra-species collisions between atoms in stretched states. For example, two atoms in the $|2, 2\rangle$ state cannot exchange spin because for every unit of spin one atom loses, the other atom must gain one unit of spin, and atoms in the $|2, 2\rangle$ already have the maximum allowed spin. For this reason, the $|2, 1\rangle$ state is the only trappable state of ^{87}Rb that can undergo spin exchange.[16, 17]

The most important mechanism for three-body losses is molecule formation. The atomic form of Rb is a meta-stable state at these densities and temperatures. It is energetically favorable for Rb to form Rb_2 molecules. In order for a molecule-forming collision to conserve both energy and momentum, however, it is necessary for a third atom to be present to carry away the binding energy of the molecule. This binding energy is much larger than the trapping potential, so both the atom and the molecule leave the trap.

Figure 4.1 summarizes the important loss mechanisms for one-, two-, and three-body losses.

4.2 Correlations

As a result of coherence the rate of inter-particle collisions is reduced in condensates compared to a gas of thermal atoms at the same density. The reason

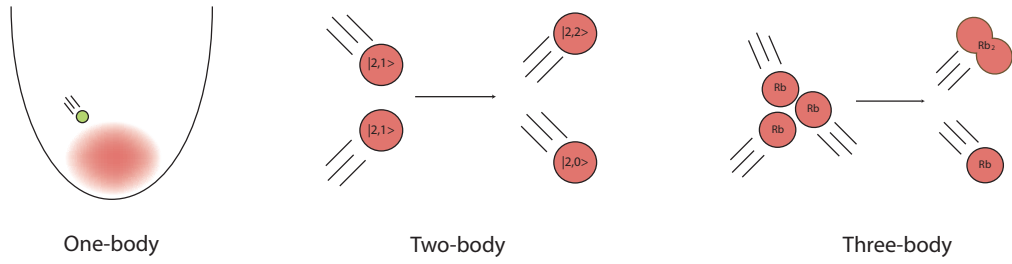


Figure 4.1: Loss mechanisms. One-body losses are caused by collisions with outside atoms or photons, two-body losses primarily by spin-exchange, and three body losses primarily by molecule formation.

for this is that the probability of m particles being close enough to one another to undergo a collision is reduced by a factor of $m!$. This effect is known as anti-bunching. Anti-bunching can be loosely understood as the result of a suppression of noise in the particle amplitude quantum field. In the noisy field of thermal atoms, a randomly chosen atom is more likely to be at a high amplitude fluctuation in the field than at a low amplitude fluctuation, but at a high amplitude fluctuation, it is more likely that a second atom and a third atom and so on will also be found near the same point. Since atoms in a condensate all occupy the single particle ground state, this noise in the particle amplitude quantum field is suppressed. [10]

This prediction is worked out in detail in Stoof *et al.* [18], and in chapter 13.2 of Pethick and Smith [4].

4.3 Measurement

We are interested in finding k_2 , the two-body loss rate, for a low density cloud of ^{87}Rb atoms in the $|2, 1\rangle$ state. In this system, there is reason to believe the first two terms in equation 4.1 dominate all following terms. Evidence for this assumption follows in the next section.

Neglecting all terms after the second, equation 4.1 becomes a solvable differential equation. We can measure density at different times as the cloud evolves, so a seemingly sensible way to proceed would be to fit these data to the solution of equation 4.1 and extract k_1 and k_2 . It turns out, however, that density-dependent losses do not completely explain the evolution of density at a given point. To understand why, take the example of a thermal cloud, which has a Gaussian density distribution. Losses due to one-body processes will simply re-scale the overall distribution, but losses due to two-body process act most strongly at the peak of the distribution, tending to flatten it out. If the distribution becomes non-Gaussian, however, the system is no longer in thermal equilibrium. As atoms collide, they will tend to re-thermalize toward a Gaussian distribution, which means that there will be a net flow of atoms toward the center of the distribution to fill the place of the lost atoms, as depicted in figure 4.2.

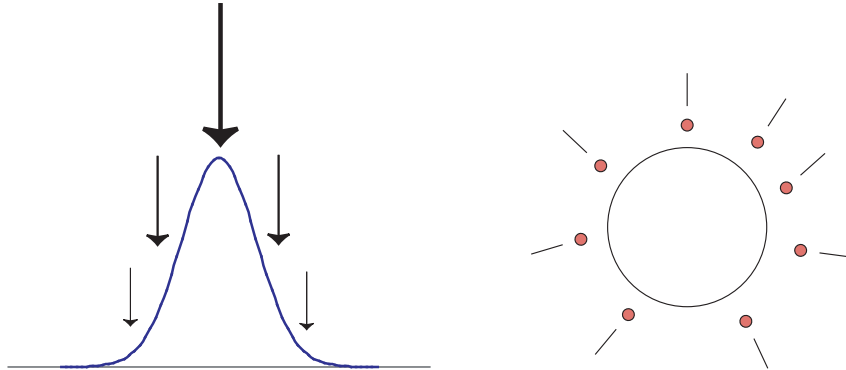


Figure 4.2: Two- and three-body loss processes cause atoms to be lost proportionally more quickly from the densest part of the cloud. As atoms rethermalize, there is a net flow of trapped atoms into the center of the cloud.

To account for this flow, we add a term $\nabla \cdot n$ to equation 4.1. There is no simple way to measure $\nabla \cdot n$ at a given point, but there is a trick to get rid of it. Integrating over all space and using Stokes' theorem, this term becomes

the flow of density out of all space, i.e. 0. It is thus generally valid to write 4.1 in integral form,

$$\int \dot{n} dv = \int (k_1 n + k_2 n^2 + k_3 n^3 + \dots) dv, \quad (4.2)$$

where the integrals are implicitly taken over all space. Integrating n over all space gives the total number, N . Additionally, the average value of a quantity a taken over all space is $\langle a \rangle = \frac{1}{N} \int n a dv$. Making these substitutions and dividing through by N gives

$$\frac{\dot{N}}{N} = \frac{d}{dt} \ln N = k_1 + k_2 \langle n \rangle + k_3 \langle n^2 \rangle + \dots \quad (4.3)$$

4.3.1 Determining Trap Lifetime

In the low density limit, all terms after the first in equation 4.3 can be ignored. Integrating the above equation in this limit gives exponential decay in the number: $\ln N/N_0 = k_1 t$, or $N = N_0 \exp(k_1 t)$. Low density thermal clouds in the $|1, -1\rangle$ or $|2, 2\rangle$ states satisfy this limit, so observing their long time decay behavior allows us to extract k_1 . Because of the rapid two-body losses in the $|2, 1\rangle$ state, it is much more difficult to measure this rate in that state. The important mechanisms for one-body losses are collisions with background gas, and absorption of stray photons. Collisions with background gas should affect all states approximately equally. If stray light from one of the lasers leaks into the cell, it could cause k_1 to differ between the $f = 1$ and $f = 2$. In any case, if these are the only important one-body loss mechanisms, the one-body loss rate measured in the $|2, 2\rangle$ state should be applicable to the $|2, 1\rangle$ state as well. $\tau = k_1^{-1}$ is referred to as the trap lifetime because it sets the overall timescale for which atoms can be trapped, regardless of internal state or magnetic field. Figure 4.3 shows a measurement of k_1 in the $|1, -1\rangle$ and $|2, 2\rangle$ states.

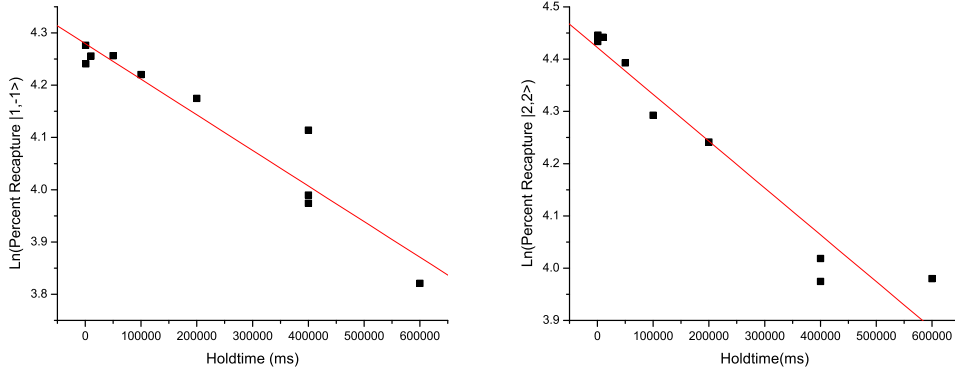


Figure 4.3: Measurement of the one-body loss rate k_1 , which is given by the slope of $\ln N$ vs. time. Recapture fraction is used as a proxy for number in these measurements. Fitting these plots to a line yields $k_{1|1,-1\rangle} = -6.8(7) \times 10^{-4} \text{s}^{-1}$ and $k_{1|2,2\rangle} = -7.4(4) \times 10^{-4} \text{s}^{-1}$. These loss rates translate into trap lifetimes of $\tau_{1,-1} = 25(3)$ minutes and $\tau_{2,2} = 23(1)$ minutes respectively.

In these measurements, atoms are loaded into the magnetic trap where they are held without any forced evaporation for varying lengths of time. These atoms are then loaded back into the MOT. This process is called recapture. Since the amount of light fluoresced by the atoms in a MOT is proportional to the total number of atoms in the MOT, using a photodiode to compare the fluorescence before and after loading the atoms into the magnetic trap allows us to determine what fraction of them were lost. It is simpler than absorption imaging for low density clouds when only relative number is needed. The measured trap lifetime of ≈ 25 minutes is significantly longer than that of many other BEC groups, and is due to excellent vacuum construction [3] and carefully built baffling to keep stray laser light out of the science cell.

4.3.2 Extracting the Two-Body Loss Rate

In denser clouds, latter terms in equation 4.3 become important. We will make the temporary assumption that in the $|2, 1\rangle$ state, at typical thermal cloud and condensate densities, all terms after the second may still be ignored. Integrating equation 4.3 and rearranging gives

$$\ln \frac{N}{N_0} - k_1 t = k_2 \int_0^t \langle n \rangle dt. \quad (4.4)$$

We image condensates at various times using absorption imaging, as explained in chapter 2, and use the measured density distributions to calculate N and $\langle n \rangle$. Using the trapezoidal approximation, we then calculate $\int_0^t \langle n \rangle dt$ for each time and plot $\ln N/N_0 - k_1 t$ vs. $\int_0^t \langle n \rangle dt$. The slope of this plot is k_2 .

4.4 Results

A serious caveat should be mentioned before data is presented. Recent discoveries suggest our determination of number and density in both condensates and thermal clouds is not accurate. The effects of saturation were not properly accounted for when the available data was taken. This problem is most severe for on resonance images. Additionally, there appears to be an asymmetry in the frequency response curve of the probing transition in condensates. At typical detunings used to image condensates, measured number is dramatically different depending on the sign of the detuning. The result of these effects is that measured number in on resonance images is almost certainly too large by up to 30%, and measured number off resonance may be too small by up to 50%. At the time of writing, the problem with the saturation correction has been solved, and we are working on taking new data and reprocessing old data. The probing asymmetry has not yet been well characterized or under-

stood. Most data, however, is taken at a single detuning and probe intensity. This means that even though absolute number and density are not well known, qualitative behavior should be correct.

Figure 4.4 shows a plot of the two-body losses in condensates and thermal clouds.

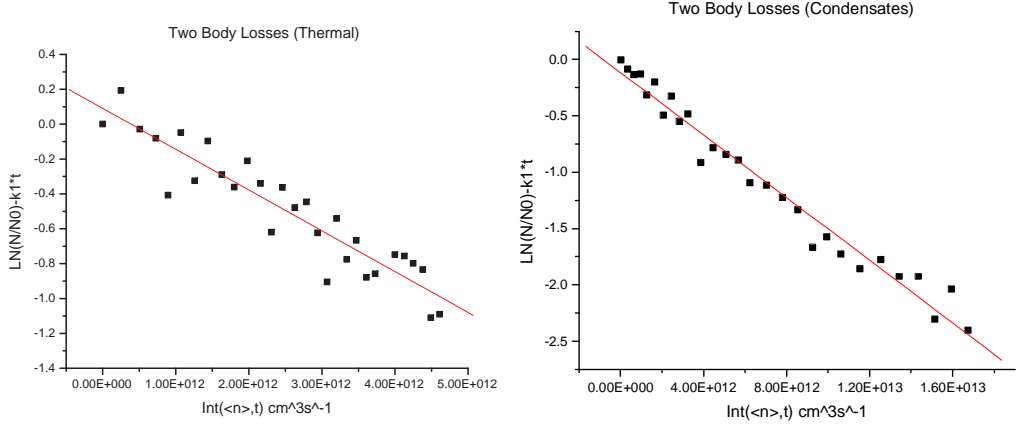


Figure 4.4: Plots of $\ln N/N_0 - k_1 t$ vs. $k_2 \int_0^t \langle n \rangle dt$ for thermal clouds and condensates, taken in a 31.3 Hz radial, 87.1 Hz axial trap. The slopes of these plots are $k_{2\text{th}}$ and $k_{2\text{c}}$, the two-body loss rate for thermal clouds and condensates respectively. Condensate data was taken 10 MHz detuned, and thermal cloud data was taken on resonance. Fitting these plots to a line produces $k_{2\text{th}} = -2.34(18) \times 10^{-13} \text{cm}^3 \text{s}^{-1}$ and $k_{2\text{c}} = -1.39(5) \times 10^{-13} \text{cm}^3 \text{s}^{-1}$. Quoted errors are statistical only; systematic errors will be considered later.

The loss rate in condensates is clearly smaller than the loss rate in thermal clouds, as predicted. The ratio of losses in thermal clouds to condensates is $k_{2\text{th}}/k_{2\text{c}} = 1.7(1)$, again using only statistical error, which is not quite consistent with the theoretically expected value of 2. It is not clear whether this discrepancy is physical or whether it is caused by one of the systematics that will be treated later in this chapter. The residuals in the thermal cloud measurement appear to be randomly distributed, but the residuals in the condensate measurement show some additional systematic. This systematic becomes

worse when a finite three-body loss rate is introduced, so it is unlikely that this effect is caused by three body losses. One possible systematic is the effect of thermal atoms also present in the trap during the condensate measurement. This effect will be considered further in section 4.5.

We now consider the question of three-body losses. Temporarily assuming that the predominant loss mechanism is a three-body process rather than a two-body process, we can extract k_3 by finding the slope of a graph of $\ln N/N_0 - k_1 t$ vs. $k_3 \int_0^t \langle n^2 \rangle dt$. Figure 4.5 shows this plot constructed from the same data as the thermal cloud plot in figure 4.4.

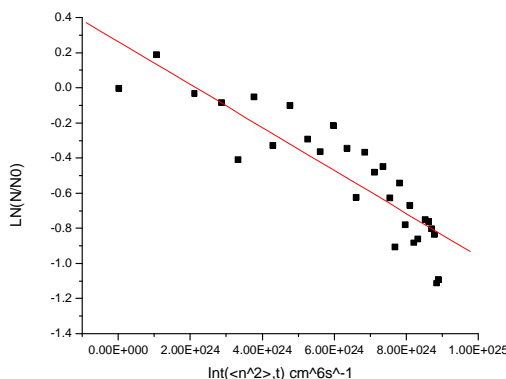


Figure 4.5: Three-body model applied to thermal clouds in the $|2, 1\rangle$ state. There appears to be some curvature to the residuals, but in this case it is difficult to discriminate with certainty between two- and three-body models based only on quality of fit. The three-body rate predicted by this plot is $k_{3\text{th}}$ is $-9.8(1) \times 10^{-25} \text{cm}^6 \text{s}^{-1}$, which is in poor agreement with theory.

The fit in figure 4.5 is worse than that in figure 4.4— $R^2 = .79$ for the three-body model and $R^2 = .86$ for the two-body model—but the quality of fit is not enough to rule out a three-body model entirely. The value of k_3 predicted by this plot, $-9.8(1) \times 10^{-25} \text{cm}^6 \text{s}^{-1}$, is four orders of magnitude larger than the values measured for the $|1, -1\rangle$ state [10], the $|2, 2\rangle$ state [19], and theoretical calculation [20, 21]. If one instead assumes, as these sources

suggest, that k_3 is of order $1 \times 10^{-29} \text{cm}^6 \text{s}^{-1}$, its effects are negligible on the time scales of measurements in both thermal clouds and condensates.

Though we work largely in a 31.3 Hz radial, 87.1 Hz axial trap because the $|1, -1\rangle$ and $|2, 1\rangle$ states overlap in this trap, working in a weaker trap appears to allow better discrimination between two- and three-body processes. Data taken this summer in a 14.6 Hz radial, 38.4 Hz axial trap puts a more stringent limit on k_3 in this state. Figure 4.6 shows a comparison of two- and three-body models for data taken in this trap.

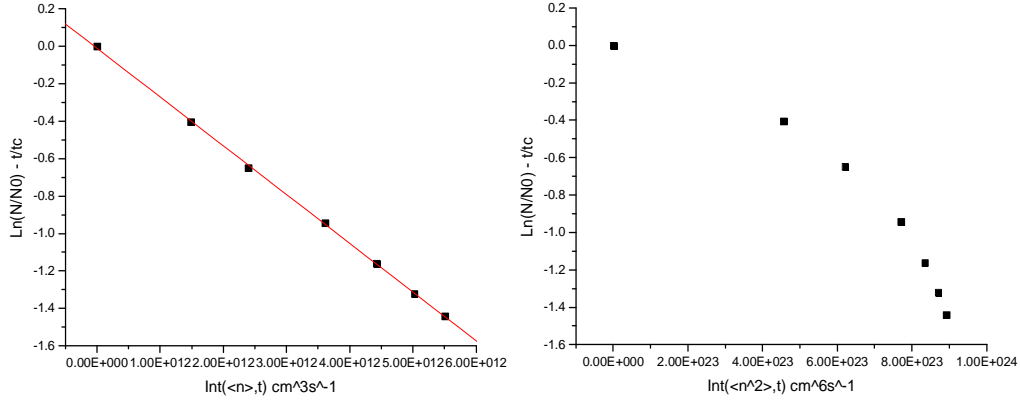


Figure 4.6: Two and three-body models applied to thermal clouds in weaker trap. In this case, the two body model is clearly much better. The two-body model gives $k_{2\text{th}} = -2.60(2) \times 10^{-13} \text{cm}^3 \text{s}^{-1}$.

Figure 4.6 appears to give a very precise measurement of $k_{2\text{th}}$, but these data were taken before the techniques of section 3.2 were developed, so an unspecified density of $|1, -1\rangle$ atoms was also in the trap when these measurements were taken.

4.5 Consideration of systematic errors

4.5.1 Improper Saturation Correction

When the correction for saturation was initially implemented this summer, the algorithm was not correct. Instead of equation 2.10, we calculated column density using

$$\sigma_0 \tilde{n}_{\text{calc}} = OD \left(1 + \Delta^2 + \frac{I_{\text{in}}}{I_{\text{sat}}} \right), \quad (4.5)$$

mistakenly using the differential form of the correction for saturation and detuning. The ratio of true column density \tilde{n} to the incorrectly calculated column density is

$$\frac{\tilde{n}}{\tilde{n}_{\text{calc}}} = \frac{OD(1 + \Delta^2) + (I_{\text{in}}/I_{\text{sat}})(1 - e^{-OD})}{OD(1 + \Delta^2 + I_{\text{in}}/I_{\text{sat}})}. \quad (4.6)$$

This ratio is always less than 1. Taking a first order expansion of the exponential, it is clear that this ratio reduces to 1 in the limit of small optical depth. Figure 4.7 shows plots of this ratio for on resonance and off resonance imaging, assuming $I/I_{\text{sat}} = 1$.

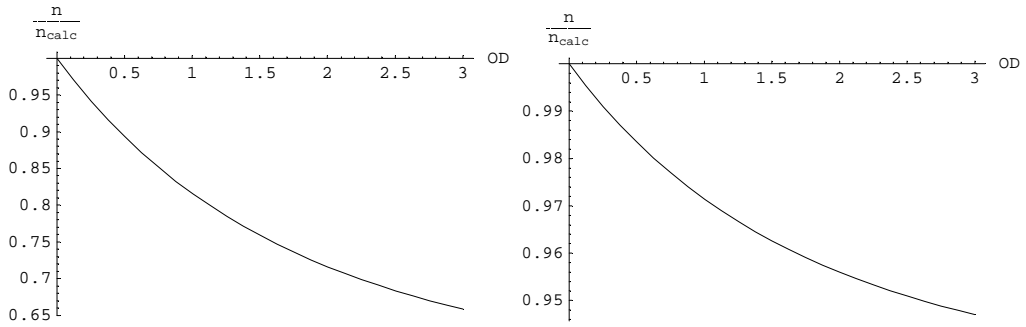


Figure 4.7: Plots of $\tilde{n}/\tilde{n}_{\text{calc}}$ for on resonance and off resonance imaging. In the first plot, $\Delta = 0$, and in the second, $\Delta = 3.3$.

The maximum optical depth typically observed on resonance is 1.5. From

the first plot in figure 4.7, it is clear that for a cloud with peak optical depth 1.5, our calculation of column density overestimated the true value by approximately 25%. Since the optical depth anywhere else in the cloud is less than the peak depth, the total number of atoms in clouds imaged on resonance was overestimated by less than 25% due to this mistake. For off resonance images, the effect is much smaller. The maximum optical depth typically observed off resonance is 2. This means that the total number of atoms in clouds imaged off resonance was overestimated by less than 4% due to this mistake.

4.5.2 Improper Correction for Detuning in Condensates

Temporarily ignoring the effects of saturation, it follows from equation 2.11 that for identically prepared condensates, N_{obs} should fall off symmetrically as a lorentzian in the detuning Δ . The probe frequency calibration curves in figure 2.1 show that this model is quite accurate for thermal clouds. It was recently discovered, however, that in condensates, N_{obs} changes dramatically with the sign of the detuning. This is true even when the condensates are observed using very low light levels, where the effects of saturation should be small. When detuned 10 MHz, N_{obs} varies by as much as a factor of two depending on the sign of the detuning. At the time of writing, this effect has not been well understood, though it may have something to do with lensing. The data appearing in this thesis was taken on the side of the resonance that produces smaller N_{obs} . It seems likely then, that N_{true} is somewhat larger than the values we calculated, though it is not clear by how much.

4.5.3 Overall Effect of Inaccuracies in Number

To determine the effect of inaccuracies in measured number, recall equation 4.4. Ignoring the effects of one-body processes, which are small over the time scales of these experiments,

$$k_2 = \frac{\ln(N/N_0)}{\int \langle n \rangle dt} \quad (4.7)$$

Consider the case in which we systematically over count the number of atoms in the condensate by some factor b so that $N_{\text{meas}} = bN_{\text{true}}$. This factor will cancel in the numerator, so only the effect on $\langle n \rangle_{\text{calc}}$ need be considered. In thermal clouds, $\langle n \rangle$ is directly proportional to N , so over counting number by a factor b will reduce the measured value of $k_{2\text{th}}$ by the same factor. Because of the improper saturation correction, it is likely that we systematically over counted the number of atoms in thermal clouds. This suggests the true value of $k_{2\text{th}}$ is likely larger than the value we measured by some factor smaller than 25%. The improper correction over counted large clouds by a larger factor than small clouds, however, so the factor will not cancel exactly in the numerator, and there will be some additional non-linear effect.

In condensates, assuming $N > 10000$ so that the Thomas-Fermi limit is valid, $\langle n \rangle$ is proportional to $N^{2/5}$ rather than N [4]. Thus if we over count N by a factor b , then $k_{2\text{c true}} = b^{2/5} k_{2\text{c meas}}$. For example, if, due to the improper correction for detuning, we under counted N so that $N_{\text{meas}} = .75N_{\text{true}}$, then $k_{2\text{c true}} = .75^{2/5} k_{2\text{c meas}} = .89 k_{2\text{c meas}}$.

4.5.4 Presence of Thermal Atoms in Condensate Measurement

At finite temperature, there is always some non-condensed fraction of atoms in the cloud. In the non-interacting limit, the condensate fraction obeys the relationship

$$\frac{N_c}{N} = 1 - \left(\frac{T}{T_c} \right)^3, \quad (4.8)$$

where T_c is the critical temperature for condensation [12, 4]. When carrying out our measurements in condensates, the thermal fraction is never readily visible. Below a certain temperature, the condensate will expand faster than the thermal fraction when dropped from the trap. This makes estimate of the thermal fraction difficult.

If thermal atoms are present, equation 4.4 must be rewritten as

$$\ln \frac{N}{N_0} - k_1 t = k_2 \int_0^t (\langle n \rangle + (2\langle n_{\text{th}} \rangle)) dt, \quad (4.9)$$

where the averages are taken over the condensate density. This form takes into account the anti-bunching of condensate atoms [19]. The right side of this equation will always be larger than the value assumed if only condensate atoms are present, causing the value of $k_{2\text{c true}}$ to be smaller than the measured value. In order to take the effects of thermal atoms into account, we would need to use warmer samples, where a thermal cloud was visible surrounding the condensate. This thermal cloud could then be fit to determine the temperature and thus the total thermal fraction.

4.5.5 Thermal Clouds Not in Equilibrium

In order for a system to remain in thermal equilibrium, the rate of elastic collisions must be large compared to the rate of inelastic collisions that cause atoms to be lost from the cloud. If this condition is not met, the thermal cloud density distribution will not remain gaussian, as shown in figure 4.2. Measured thermal cloud distributions are still well described by gaussians after undergoing expansion, but it would be difficult for us to measure small deviations from this distribution. If the thermal cloud density distribution in the trap deviates from a gaussian, then our calculation of $\langle n \rangle$ in thermal clouds would no longer be correct. Since a gaussian density distribution remains a good fit

to thermal cloud density distributions after expansion to the best of our ability to measure, it is likely that this would be a small correction

4.6 Conclusions

Due largely to improper correction for saturation, there is a systematic uncertainty in the range of 20% in our measurement of the two-body loss rate in thermal clouds. We are thus able to quote $k_{2\text{th}} = -2.34(\pm.18 \pm .47) \times 10^{-13}$ in 31.3 Hz radial, 87.1 Hz axial trap where the first number represents statistical error only, and the second number represents systematic effects. It is likely that the true number lies on the high side of this range. Until the effects of detuning are better understood in condensates, it seems unwise to quote a final number for k_{2c} . It seems likely that the true value lies somewhere below our measured value. Our measurements are thus consistent with a factor of two suppression of two body losses in condensates, though they do not yet provide a strong test of this factor of two.

It seems likely that, using the techniques explained in this thesis, we will soon be able to quote an accurate value of the two-body loss rate in the overlap trap where we are working on measuring it. We may also soon be able to apply these techniques to $|1, -1\rangle$ and $|2, 2\rangle$ clouds in order to set better constraints on the three body loss rate in these systems. For further study, it would be interesting to study the relationship of the two-body loss rate to magnetic field by carrying out the measurement in a variety of different traps, especially in the region of a Feshbach resonance, where inelastic loss rates are expected to have a very strong dependence on small changes in the magnetic field [16, 22, 23].

Bibliography

- [1] Mark Henry Wheeler. A new observation of matter-wave interference in binary bose-einstein condensates, 2004.
- [2] Theodore James Reber. Creating and optically trapping a bose-einstein condensate of rubidium 87, 2003.
- [3] Benjamin J. Samelson-Jones. Vacuum construction and magneto-optic trapping for bose-einstein condensation, 2001.
- [4] C. J. Pethick and H. Smith. *Bose-Einstein Condensation in Dilute Gases*. Cambridge University Press, New York, NY, 2002.
- [5] M. R. Matthews, D. S. Hall, D. S. Jin, J. R. Ensher, C. E. Wieman, and E. A. Cornell. Dynamical response of a bose-einstein condensate to a discontinuous change in internal state. *Physical Review Letters*, 81(2):243–247, 1998.
- [6] D. S. Hall, M. R. Matthews, C. E. Wieman, and E. A. Cornell. Measurements of relative phase in two-component bose-einstein condensates. *Physical Review Letters*, 81:1543–1546, 1998.
- [7] D. S. Hall, M. R. Matthews, J. R. Ensher, C. E. Wieman, and E. A. Cornell. Dynamics of component separation in a binary mixture of bose-einstein condensates. *Physical Review Letters*, 81:1539–1542, 1998.

- [8] Mark H. Wheeler, Kevin M. Mertes, Jessie D. Erwin, and David S. Hall. Spontaneous macroscopic spin polarization in independent spinor bose-einstein condensates. *Physical Review Letters*, 93:170402, 2004.
- [9] M. R. Andrews, C. G. Townsend, H. J. Miesner, D. M. Kurn, and W. Ketterle. Observation of interference between two bose condensates. *Science*, 275:637–641, 1997.
- [10] E. A. Burt, R. W. Ghrist, C. J. Myatt, M. J. Holland, E. A. Cornell, and C. E. Wieman. Coherence, correlations, and collisions: What one learns about bose-einstein condensates from their decay. *Physical Review Letters*, 79:337–340, 1997.
- [11] A. E. Siegman. *Lasers*. University Science Books, Sausalito, CA, 1986.
- [12] Jason Remington Ensher. *The First Experiments with Bose-Einstein Condensation of ^{87}Rb* . PhD thesis, University of Colorado, 1998.
- [13] Jacob Lyman Roberts. *Bose-Einstein Condensates with Tunable Atom-atom Interactions: The First Experiments with ^{85}Rb BECs*. PhD thesis, University of Colorado, 2001.
- [14] U. Volz and H. Schmoranzner. Precision lifetime measurements on alkali atoms and on helium by beam-gas-laser spectroscopy. *Physica Scripta*, T65:48, 1996.
- [15] M. O. Mewes, M. R. Andrews, D. M. Kurn, D.S. Durfee, C. G. Townsend, and W. Ketterle. Output coupler for bose-einstein condensed atoms. *Physical Review Letters*, 78:582–585, 1997.

- [16] E. Tiesinga, B. J. Verhaar, and H.T.C. Stoof. Threshold and resonance phenomena in ultracold ground-state collisions. *Physical Review A*, 47(5):4114–4122, 1992.
- [17] John Weiner, Vanderlei S. Bagnato, Sergio Zilio, and Paul S. Julienne. Experiments and theory in cold and ultracold collisions. *Reviews of Modern Physics*, 71(1), 1999.
- [18] H. T. C. Stoof, A. M. L. Janssen, J. M. V. A. Koelman, and B.J. Verhaar. Decay of spin-polarized atomic hydrogen in the presence of a bose condensate. *Physical Review A*, 39(6), 1998.
- [19] J. Söding, D. Guéry-Odelin, P. Desbiolles, F. Chevy, H. Inamori, and J. Dalibard. Three-body decay of a rubidium bose-einstein condensate. *Applied Physics B*, 69:257–261, 1999.
- [20] P. Fedichev, M. Reynolds, and G. V. Shlyapnikov. Three-body recombination of ultracold atoms to a weakly bound s level. *Physical Review Letters*, 77, 1996.
- [21] A. J. Moerdijk, H. M. J. M. Boesten, and B. J. Verhaar. Decay of trapped ultracold alkali atoms by recombination. *Physical Review A*, 53, 1996.
- [22] E. G. M. van Kempen, S. J. J. M. F. Kokkelmans, D. J. Heinzen, and B. J. Verhaar. Interisotope determination of ultracold rubidium interactions from three high-precision experiments. *Physical Review Letters*, 88(9):93201–1, 2002.
- [23] Thomas Volz, Stephan Dürr, Sebastian Ernst, Andreas Marte, and Gerhard Rempe. Characterization of elastic scattering near a feshbach resonance in ^{87}rb . *Physical Review A*, 68:010702–1, 2003.